RESEARCH ARTICLE

Influence of the Inherited Structure Induced by Al and Si Alloying on Microstructure Evolution and Mechanical Properties of 100Cr6 Steels

Tarek Allam,* Pascal Ostermayer, Bastian Blinn, Tilmann Beck, and Wolfgang Bleck

The fatigue lifetime of high-strength 100Cr6 steels can be improved by an increased content of retained austenite that can be induced by Al and Si alloying. The related deformation-induced retention of the austenite–martensite transformation during cyclic loading increases their local strain hardening capacity. However, for those 100Cr6 steels containing retained austenite, sufficient dimensional stability must be ensured. In this study, two standard 100Cr6 steels alloyed either with 1.5 wt% Al or 1.5 wt% Si (to diminish carbide formation and accordingly promote austenite retention) are laboratory melted and processed to adjust a microstructure of bainite, retained austenite, and carbides. The segregation simulation in the as-cast condition and the corresponding microstructures in the forging and heat-treating conditions are investigated. The inheritance of chemical heterogeneity leads to structural heterogeneity on both the nano- (nm) and micro (µm) scales. This heterogeneity is much more pronounced in the Al-alloyed steel, which can be attributed to inheritance from the as-cast state. While the results of the quasistatic tensile tests are comparable for both alloys, the cyclic load increase tests indicate a higher fatigue strength of the Si-alloyed steel, which can be explained with the more homogenous microstructure and the finer distribution of the retained austenite.

T. Allam, W. Bleck
Steel Institute
RWTH Aachen University
52056 Aachen, Germany
E-mail: t.allam@fz-juelich.de

T. Allam
Department of Metallurgical and Materials Engineering
Suez University
Suez 43528, Egypt

P. Ostermayer, B. Blinn, T. Beck
Institute of Materials Science and Engineering
TU Kaiserslautern
67663 Kaiserslautern, Germany

The ORCID identification number(s) for the author(s) of this article can be found under https://doi.org/10.1002/srin.202200804.

1. Introduction

For common applications, the roller-bearing steel 100Cr6 (materials number 1.3505, EN ISO 683-17, SAE 52100) is used in conditions with a martensitic microstructure containing $\approx$6–10 vol% retained austenite. As shown in another study,[1] the retained austenite in 100Cr6 can transform to α'-martensite, which depends on the applied loadings and the stability of the retained austenitic phase. In this context, the content as well as the stability of the retained austenite strongly depend on the preceding heat treatment.[2,3] As shown in other studies,[4–6] this deformation-induced phase transformation significantly increases the damage tolerance of a material, as it suppresses the initiation and propagation of fatigue cracks and thus increases the fatigue lifetime.[7,8] Besides the positive effect of the retained austenite on the lifetime of roller bearings reported in other studies,[9,10] the austenite-α'–martensite transformation can lead to undesired changes in the dimensions of the components as a result of tempering or under operating conditions.[1] The volume fraction, distribution, and stability of the retained austenite determine the deformation-induced austenite-α'–martensite transformation as a function of the temperature and the mechanical stress.[11] These parameters must be chosen in such a way that, on the one hand, the intended increase in the damage tolerance is achieved, but on the other hand a large-scale transformation, and thus, a volume change that exceeds the geometrical tolerance, is excluded.[12]

Based on the classical alloy concept of 100Cr6 steel,[13] the retained austenite stability can be controlled by the Al and Si content. Both chemical elements play an important role for this alloy, since Si ensures a high level of cleanliness of the material[1] and Al improves the spheroidization and suppresses the formation of cementite networks.[14] Moreover, aluminum nitrides support the stability of fine grains during heat treatment, which can also be beneficial for mechanical properties. However, high Al contents can also lead to a pronounced formation of oxide inclusions and, thus, might result in a lower cleanliness of the material.[15] Considering the austenite stability, it was reported that Si increases the thermal and mechanical stability of the austenitic phase in 100Cr6.[16] Moreover, it has been shown that Si

suppresses the carbide formation during bainitization, which leads to a higher carbon content in the retained austenite after cooling and, hence, a higher austenite stability. Besides the effect of deoxidation, Al binds N and suppresses cementite formation in a similar way to Si,[15] which also results in a higher stability of the retained austenite. In addition to the effect of the alloying elements, it was found that retained austenite in the form of a film located between the bainite plates is more stable than the retained austenite in coarser blocks.[17]

Consequently, in this work, the influence of the Si and Al content on the evolution of the microstructure of 100Cr6, especially on the formation of retained austenite, is investigated. To thoroughly analyze the influence of Al and Si on the retained austenite formation, two modifications of 100Cr6, which contain a higher content of Si or Al, were investigated. In this context, the development of the microstructure and of the local chemical composition during processing are examined. A special focus is placed on the formation of structural heterogeneities as well as the relation of the microstructure and the resulting monotonic and cyclic deformation behavior.

2. Experimental Section

2.1. Materials

Two laboratory-scale 100Cr6 steel melts were produced via a process route consisting of vacuum-induction melting, ingot casting, and hot forging. While one steel was alloyed with a relatively high content of Al of 1.5 wt%, the other steel contained 1.5 wt% Si. Thus, the alloys will hereafter be called 1.5Al–100Cr6 and 1.5Si–100Cr6 and their chemical compositions are listed in **Table 1**. To homogenize the cast ingots (550 × 140 × 140 mm^3), a stepwise heating up to 1250 °C was conducted before hot forging. Therefore, a slow heating rate of 1.5–2 K min^{-1} and holding times of 2 h at each heating step (300, 600, 900, and 1250 °C) were applied. The hot forging was performed in the high-temperature range between 1250 and 1050 °C in several steps, combined with intermediate reheating. The forged bars with a final cross section of 80 × 80 mm^2 were cooled in a furnace from 1100 to ≈400 °C followed by air cooling. A schematic representation of the applied stepwise heating, hot forging, and cooling procedures is shown in **Figure 1**a.

Subsequent to forging, an austenitization and bainitization of both steels were applied in dilatometer experiments. The austenitization step at 900 °C (30 min for 1.5Al–100Cr6 and 60 min for 1.5Si–100Cr6) was followed by a rapid cooling to the bainitizing temperature of 240 °C, which was held for 8 h to achieve the bainitized microstructure (comp. Figure 1b). In addition, the solution-treated microstructure was characterized after quenching from austenitization temperature. Note that the heat treatment parameters were chosen based on a parameter analysis,
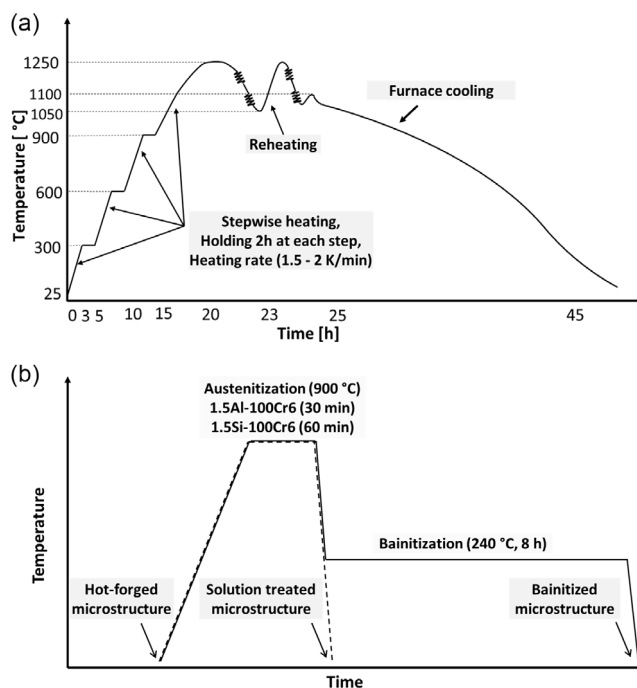
Figure 1. Preparation of the investigated 1.5Al– and 1.5Si–100Cr6 steels. a) Schematic representation of the stepwise heating, hot forging, and cooling procedures as well as b) the applied heat treatment regimes in dilatometer experiments.

which is described in detail for 1.5Si–100Cr6 in another study[18] and was performed analogously for 1.5Al–100Cr6. To produce the fatigue and tensile specimens, the heat treatment, which was done at IWT Bremen, was performed in a salt bath, as these specimens had a significantly bigger volume.

2.2. Thermodynamic Calculations and Microstructure Simulation during Solidification

A Scheil-solidification calculation was conducted for both steels under consideration that C is the fastest diffusing element. For this purpose, the database TCFE Steels/Fe-alloys version 9 was applied during the thermodynamic calculations using the Thermo-Calc software package. Accordingly, the evolution of the solid fraction and the corresponding change in chemical composition, as well as the partitioning of alloying elements during solidification, were predicted. Moreover, the microstructures of the solidified Al- and Si-alloyed 100Cr6 steels were simulated using the microstructure evolution simulation software (MICRESS) version 7.003 with an enabled Thermo-Calc coupling. 2D calculations were performed using a grid size of 400 × 400 cells with a grid spacing of 2 μm. The FCC_A1 (austenite) was specified as the solid phase that formed from the liquid phase at a cooling rate of 0.2 K s^{-1} during solidification simulation, considering periodic boundary conditions.

2.3. Characterization of Microstructural Features

Various investigation techniques were applied to analyze the differences induced by Al and Si alloying in microstructural

Table 1. The chemical composition of the investigated steels in wt%.

Steels	C	Si	Mn	P	S	Cr	Ni	Al	N	O
1.5Al–100Cr6	1.00	0.31	0.43	0.003	0.002	1.49	0.2	1.51	0.003	0.0006
1.5Si–100Cr6	1.00	1.51	0.43	0.003	0.002	1.49	0.2	0.031	0.003	0.0008

characteristics of 100Cr6 steels. For both steels, the forged microstructure was examined using a light optical microscope (LOM) and a field-emission scanning electron microscope (SEM) on metallographically prepared specimens to view the general grain structure and the presence of secondary cementite at the grain boundaries. The specimens were prepared by mechanical grinding using abrasive paper up to 1200 grit and subsequently polished with a diamond suspension of 3 and finally, 1 μm. The microstructures were revealed using 3% nital etching solution. Furthermore, the presence and distribution of carbides in the heat-treated microstructures were investigated using SEM. Therefore, a Zeiss Gemini SEM (Carl Zeiss Microscopy GmbH, Germany) was operated at an accelerating voltage of 15–20 kV and a working distance of 10–30 mm.

Moreover, the retained austenite in the bainitized microstructure was analyzed by means of electron backscatter diffraction (EBSD) technique. A detector of type EDAX-TSL Hikari was used to record the EBSD maps performed with a step size of 50 nm. The analysis and visualization of EBSD data were conducted using a software package from Aztec (Version 3.3, Oxford Instruments, Oxford, UK). The employed specimens for EBSD measurements were prepared according to the standard metallographic mechanical grinding and polishing procedures followed by electropolishing, which were performed at ambient temperature for 20 s at 36 V in a commercial electrolyte consisting of 700 mL ethanol, 100 mL butyl glycol, and 78 mL 60%-perchloric acid.

2.4. Measurement of the Retained Austenite Fraction by Means of X-ray Diffraction

In addition to the EBSD analysis, the fraction of retained austenite was determined by X-ray diffraction (XRD) measurements with a diffractometer of type "MZ VI E" from General Electric, using Cr-Kα radiation and an aperture of 1 mm. The diffraction patterns were then analyzed using the Rietveld method for determining the retained austenite content, whereas goodness of fit values of 1.03 for the 1.5Si–100Cr6 and 1.04 for the 1.5Al–100Cr6 were achieved. The measurements were performed in the center of a wire erosion-prepared cross section of the dilatometer specimens, whereby 30 μm of the material was electrolytically removed to eliminate the influences of the preparation process. The austenite fractions determined can be given with a standard deviation of three percentage points. Note that the XRD analysis was performed by our project partner, Leibniz-Institute IWT Bremen.

2.5. Characterization of Quasistatic and Cyclic Properties

Tensile and fatigue tests were performed to analyze the quasistatic and cyclic properties of both steels. The tensile tests were performed strain controlled according to DIN EN ISO 6892[19] at ambient temperature using a universal testing machine of type 112 from TesT GmbH and tensile specimens with the geometry given in **Figure 2**a. For strain measurement, a tactile extensometer with an initial gauge length of 25 mm was used. Note that the tensile test results were based on two specimens for each alloy.

To characterize the cyclic deformation behavior, uniaxial load increase tests (LIT) were conducted stress controlled at ambient temperature with a servohydraulic testing system of type Schenck PSA 40 kN, using a frequency of $f = 10$ Hz and a stress ratio of $R = -1$. Using the same test parameters, initial constant amplitude tests were carried out based on the results of the LIT at high and medium stress amplitudes, respectively. The fatigue specimens had the geometry given in Figure 2b and a polished gauge length. The LIT started at a stress amplitude of $\sigma_{a,start} = 300$ MPa, which was stepwise increased by $\Delta\sigma_a = 20$ MPa in intervals of $\Delta N = 9 \times 10^3$ cycles. To measure the cyclic strain, a strain gage-based extensometer with an initial gauge length of 8 mm was used. As shown in another study,[6] these high-strength steels showed a relatively low amount of plastic deformation, and thus, a measurement of the deformation-induced change in temperature enabled a higher resolution of the cyclic deformation behavior. Note that the area of the stress–strain hysteresis represents the deformation energy applied in each cycle, which dissipates mostly to heat.[20] Thus, an increase of the temperature in the gauge length corresponds to a more pronounced cyclic plastic deformation.[21] Using higher frequencies, more deformation energy dissipates at the same time and, hence, also small plastic deformation leads to a change in temperature, resulting in a higher resolution of the cyclic deformation behavior.

To determine the deformation-induced change in temperature ΔT, the temperatures in the middle of the gauge length (T_1) and at the clamping shafts of the specimens (T_2 and T_3) were measured with thermocouples. While T_1 detected the temperature increase caused by plastic deformation, T_2 and T_3 were used to filter changes in the environmental temperature. Therefore, ΔT was calculated with Equation (1) in accordance with[20]

$$\Delta T = T_1 - \frac{T_2 + T_3}{2} \tag{1}$$
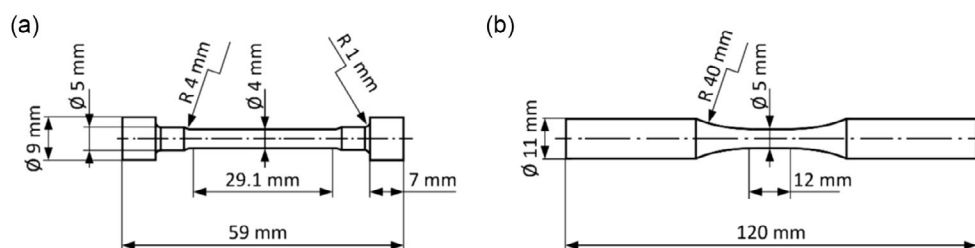
Figure 2. Geometry of the a) tensile and b) fatigue specimens.
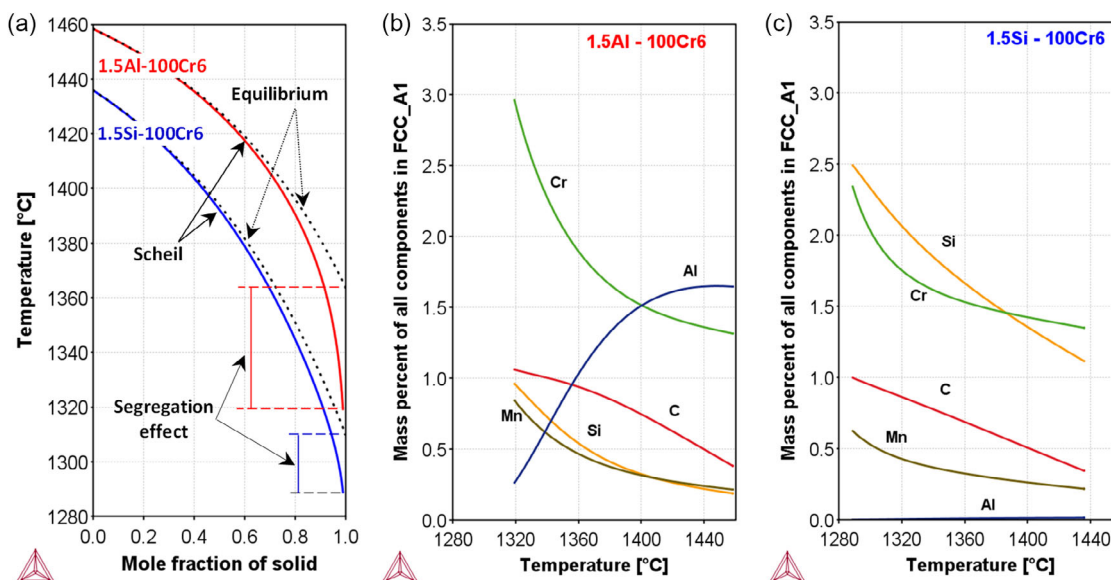
Figure 3. Scheil-solidification calculation. a) Evolution of solid fraction of 1.5Al–100Cr6 and 1.5Si–100Cr6 steels. b,c) Concentration of alloying elements in solid phase (represented by mass percent of all components in FCC_A1) during solidification for (b) 1.5Al–100Cr6 and (c) 1.5Si–100Cr6.

3. Results

3.1. Scheil-Solidification Calculation and Solidified Microstructure Simulation

The evolution of solid fraction with respect to the temperature and the relative concentration of alloying elements in the solid phase during solidification were calculated by means of Scheil-solidification module in Thermo-Calc. The results are displayed in **Figure 3**. Under nonequilibrium solidification conditions, the segregation of alloying elements expands the solidification temperature range and decreases the solidus temperature. Accordingly, the impact of Al and Si alloying on the extent of segregation of elements in both 1.5Al–100Cr6 and 1.5Si–100Cr6 steels can be analyzed by comparing the equilibrium solidification (dashed lines) with the Scheil-solidification (solid lines) in Figure 3a. It is observed that the deviation from equilibrium solidification is larger and the decrease in solidus temperature is more pronounced in 1.5Al–100Cr6 than those observed for 1.5Si–100Cr6. Moreover, the continuous increase in concentration of alloying elements (C, Si, Mn, and Cr) in the solid FCC_A1 phase (austenite) during solidification of 1.5Al–100Cr6 shown in Figure 3b implies the rejection of these elements in front of the advancing solid. In contrast to the concentration profiles of C, Si, Mn, and Cr, the Al concentration decreases in the solid phase until the end of solidification. A similar segregation behavior of alloying elements is observed for 1.5Si–100Cr6 (Figure 3c). However, the extent of segregation is lower than for 1.5Al–100Cr6.

Table 2 represents the segregation factors compiled from the Scheil-solidification calculations of both steels based on the highest and lowest concentrations of alloying elements in the solid phase (FCC) during solidification (from Figure 3b). In addition, **Figure 4** shows that the Mn and Cr partitioning coefficients for 1.5Al–100Cr6 steel are lower than their counterparts for

Table 2. Segregation factors of alloying elements based on the concentrations of alloying elements compiled from scheil-solidification calculations of both of the 1.5Al–100Cr and 1.5Si–100Cr6 steels based on the highest and lowest concentration of each alloying element in the solid phase (FCC) during solidification.

Steels	Segregation factor (highest-%/lowest-%)			
	Mn	Cr	Al	Si
1.5Al–100Cr6	4.25	2.3	6.8	4.7
1.5Si–100Cr6	3	1.7	–	2.3
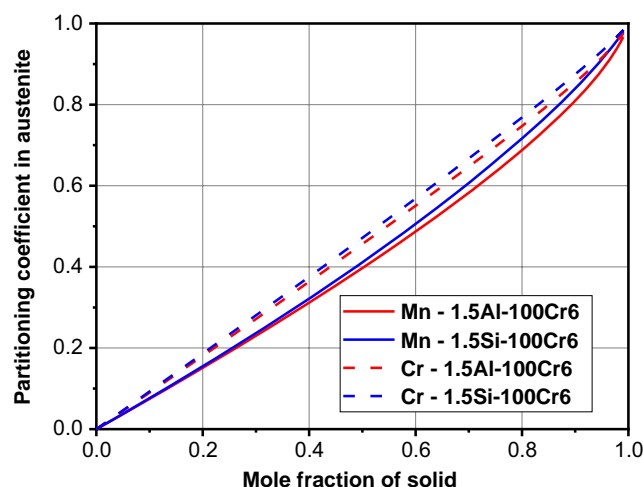
Figure 4. Partitioning coefficient between liquid and solid phases of Mn and Cr during solidification of 1.5Al–100Cr6 and 1.5Si–100Cr6 steel derived from Scheil-solidification calculations.

1.5Si–100Cr6 steel. The partitioning coefficient of an alloying element (K_i) is represented by its relative distribution between solid (C_s^i) and liquid (C_l^i) phases during solidification and is compiled from the Scheil-solidification calculation according to Equation (2).
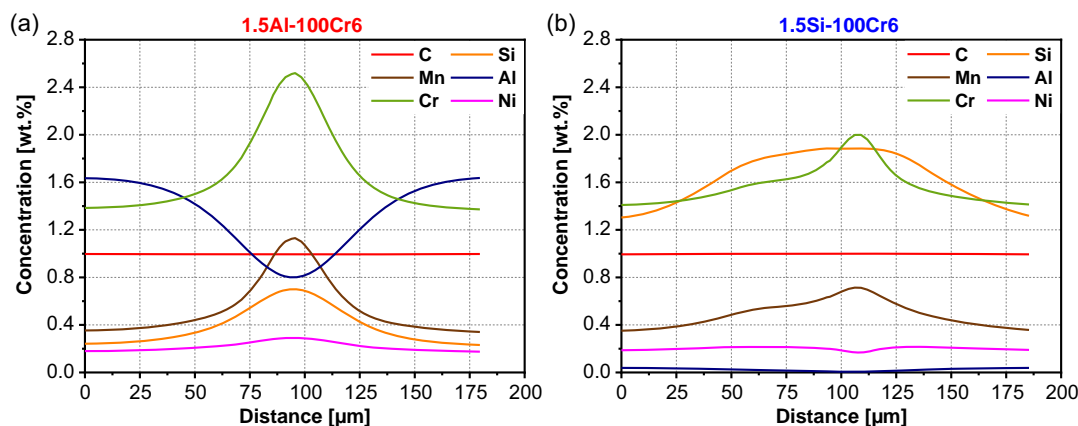
$$K_i = \frac{C_s^i}{C_l^i} \tag{2}$$

A lower partitioning coefficient of an element indicates a lower solubility in the solid phase and accordingly a higher tendency to segregate.[22] Based on these simulation results, 1.5Al–100Cr6 reveals a stronger segregation tendency of alloying elements during solidification in relation to 1.5Si–100Cr6 steel.

The distribution of alloying elements in the solidified microstructure of both Al- and Si-alloyed 100Cr6 steels was simulated using MICRESS, which is presented in **Figure 5**. The color-code scale shows the variation in content of the alloying elements between the dendritic and interdendritic solidified regions. The concentration profile of each alloying element between
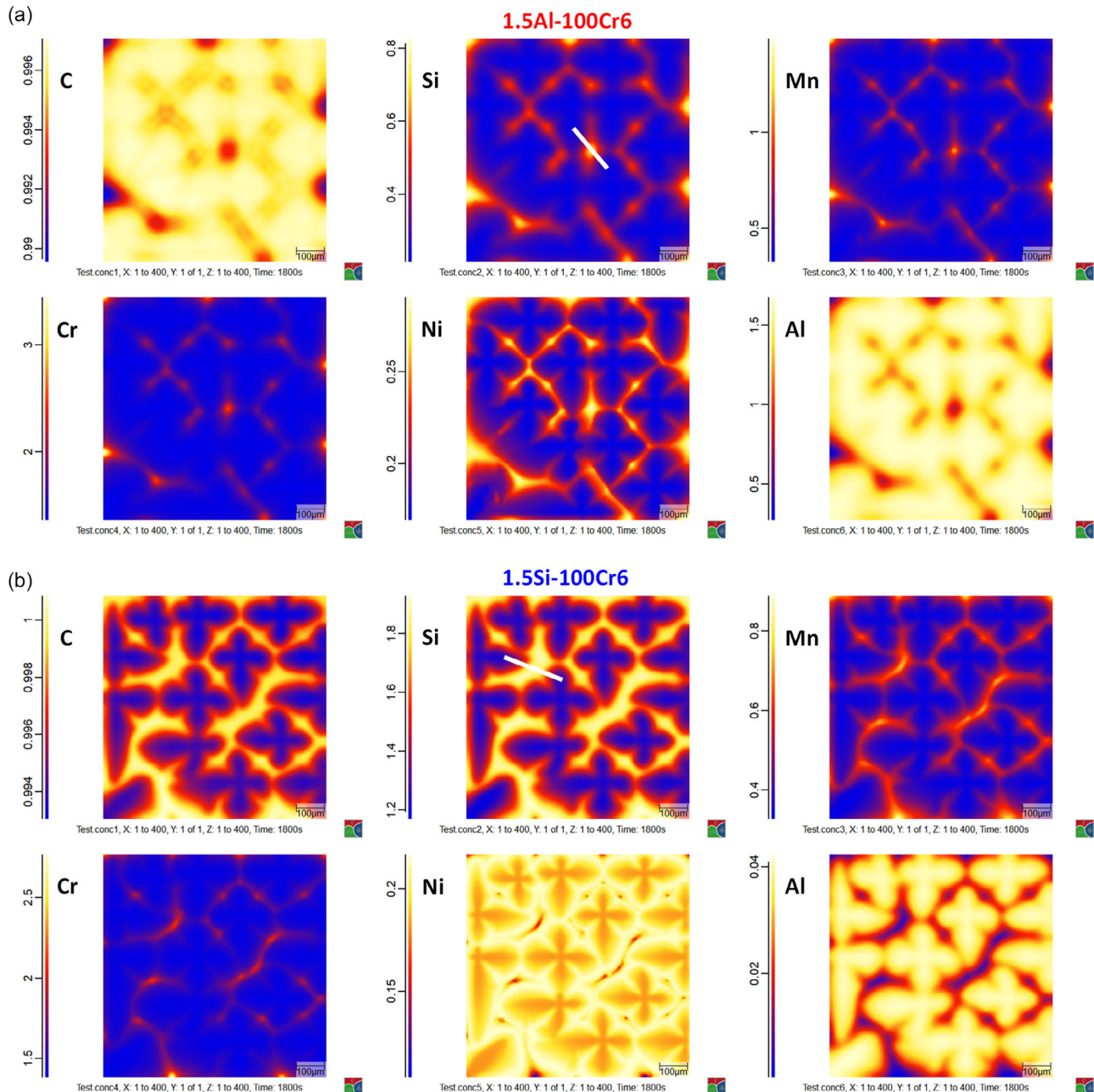
Figure 5. Distributions of alloying elements in solidified microstructures of a) 1.5Al–100Cr6 and b) 1.5Si–100Cr6L using microstructure evolution simulation software (MICRESS). The graphical representations are for a simulation grid of 400 × 400 cells showing the distribution of C, Si, Mn, Cr, Ni, and Al at 1800 s for each steel.

ADVANCED
SCIENCE NEWS

www.advancedsciencenews.com

steel
research
international

www.steel-research.de

Figure 6. Concentration profiles of alloying elements across the solidified interdendritic region, indicated by white solid lines on the simulated microstructure using MICRESS in **Figure 5**, for a) 1.5Al–100Cr6 and b) 1.5Si–100Cr6. The lines start from a dendritic arm crossing over interdendritic region to the neighboring dendritic arm.

two dendritic arms crossing an interdendritic region was compiled from the simulated compositional data, which is indicated by the white lines in Figure 5 and displayed as line scans in **Figure 6**. The concentration profiles of C and Ni exhibit only marginal changes from the dendritic to the interdendritic regions of both steels. In agreement with the Scheil-solidification calculations, the concentration profiles of Cr and Mn in 1.5Al-100Cr6 steel reveal a greater tendency for segregation in the interdendritic region than their counterparts in 1.5Si–100Cr6 steel. Moreover, Si tends to be enriched (cosegregated) in the interdendritic regions of both steels, and the corresponding enrichment level depends on the original Si content. However, the concentration profile of Al shows an opposite segregation behavior to other alloying elements, since it is depleted in the interdendritic region and enriched in the dendritic one.

It is worth noting that the results from Scheil-solidification calculations and simulation of solidified microstructure using

MICRESS indicate, in addition to the pronounced difference in the level of enrichment of carbide forming/stabilizing elements, that is, Cr and Mn, an opposite partitioning behavior of Al and Si in both steels. Such predicted differences in the distribution of alloying elements inherited from the initial solidified microstructure between Al- and Si-alloyed 100Cr6 steels are supposed to influence their microstructure evolution during subsequent heat treatments, which will be shown in the following sections.

3.2. Microstructural features of the As-Forged state

Characteristics of the as-forged microstructure of both steels were revealed by means of LOM and SEM and are presented in **Figure 7**. Generally, both steels exhibit fully pearlitic microstructures containing various typical pearlite colonies of different
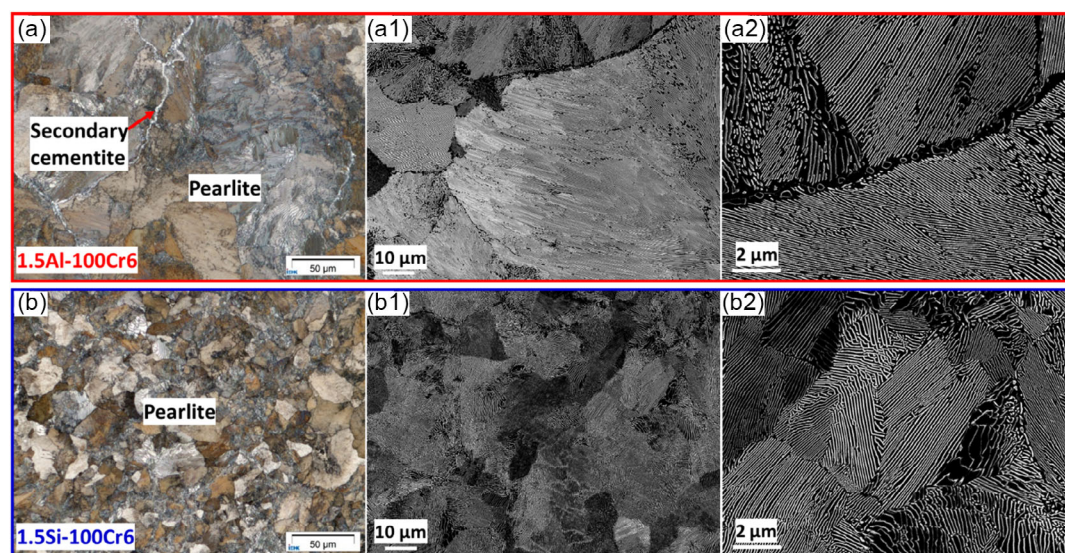
Figure 7. LOM and SEM micrographs of the as-forged microstructure. a), a1) and a2) for 1.5Al–100Cr6 and b), b1) and b2) for 1.5Si–100Cr6.

orientations, as can be seen in Figure 7a,b. Obviously, the microstructure in the as-forged state of 1.5Al–100Cr6 steel shows a coarse pearlitic grain structure with a size of several tens of micrometers accompanied with thin films of secondary cementite, which are considerably present along the grain boundaries. Compared with 1.5Al–100Cr6 steel, the 1.5Si–100Cr6 steel possesses a finer grain structure without indications of secondary cementite on the grain boundaries. The same characteristics were observed from the SEM micrographs in Figure 7a1,a2 and b1,b2, which display the pearlitic microstructure at higher magnification in the as-forged state with an average estimated pearlite lamella spacing of around 0.33 and 0.22 μm for 1.5Al–100Cr6 and 1.5Si–100Cr6 steels, respectively.

3.3. Evolution of the Microstructural Features during Heat Treatment
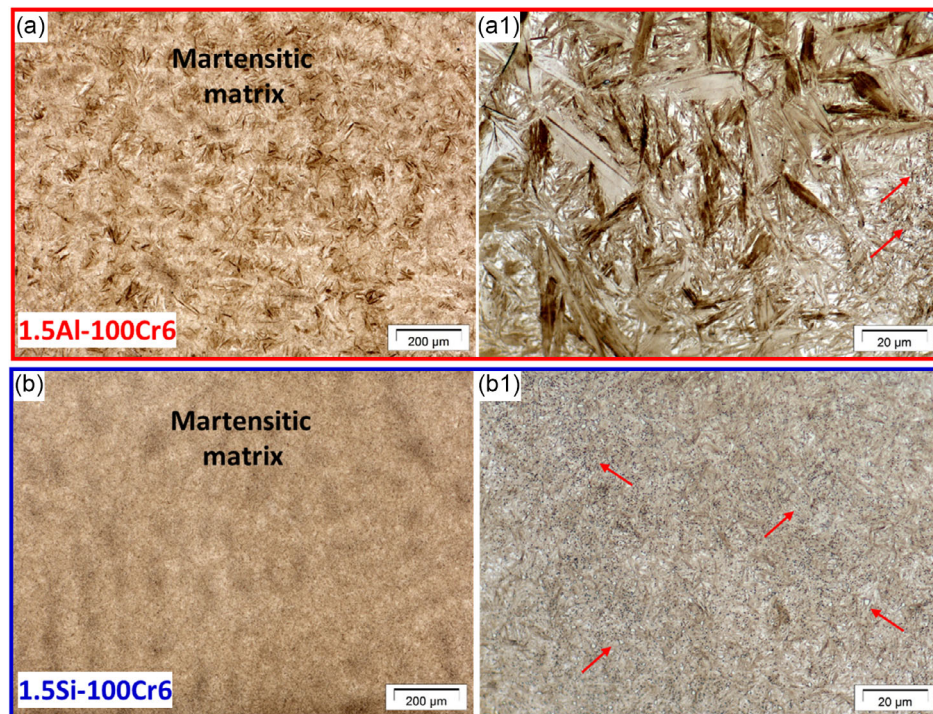
3.3.1. Solution-Treated Microstructure

Figure 8 displays the solution-treated microstructures of the 1.5Al–100Cr6 and 1.5Si–100Cr6 steels. The LOM micrographs of both steels shown in Figure 8a,b reveal the presence of elemental segregation indicated by the difference in etching contrast, which is accepted as a common characteristic of alloyed steels. Furthermore, the comparison of Figure 8a1,b1 evidences the coarse nature of the constituting martensite phase in 1.5Al–100Cr6 steel in relation to the martensite of 1.5Si–10Cr6 steel. Moreover, a closer inspection of the microstructure of both steels indicates the presence of carbides with different sizes and arrangements, which is described in more detail below.

The localization and distribution of the carbides were investigated by means of SEM, which is illustrated in **Figure 9**. The overview micrograph in Figure 9a shows a localization of the carbides for 1.5Al–100Cr6, since few regions manifest the presence of clusters of carbides (green arrows), whereas the other regions are almost free of carbides (orange arrows). These features are emphasized further in Figure 9a1. Besides the clusters of carbides, it seems that the cementite particles did not completely dissolve at the applied austenitization temperature, as some elongated and relatively large particles are still observed. For 1.5Si–100Cr6 steel, the clusters of carbides are randomly distributed in the microstructure (Figure 9b1), and a considerable amount of cementite particles is present.

The presented LOM and SEM observations demonstrate that the solution-annealed microstructure of Al1.5–100Cr6 steel can be qualitatively distinguished from that of 1.5Si–100Cr6 steel in terms of the size of constituting martensite, the distribution of carbide clusters, and the amount of cementite particles.
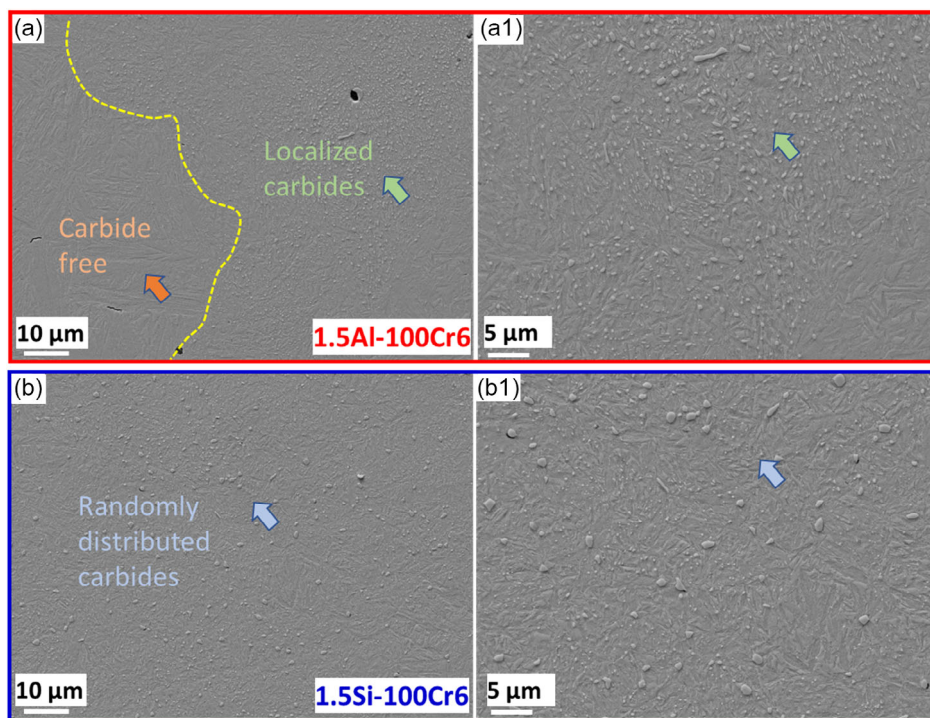
3.3.2. Bainitized Microstructure

The microstructure that results from the bainitization heat treatment was characterized using LOM, SEM, and EBSD, which enables the analysis of the impact of the inherited microstructure induced by Al and Si alloying. The LOM images shown in **Figure 10**a,b are overviews of the microstructures of 1.5Al–100Cr6 and 1.5Si–100Cr6 steels after the bainitization heat treatment. Both steels exhibit a bainitic microstructure containing carbides as well as cementite particles. The observed bainite plates for 1.5Al–100Cr6 steel are significantly coarser in relation


Figure 8. LOM micrographs of the solution-annealed microstructure for a) 1.5Al–100Cr6 steel and b) 1.5Si–100Cr6 steel. a1,b1) Recorded at a relatively higher magnification. The red arrows indicate the present carbides in different arrangements and sizes.

Figure 9. SEM micrographs of the solution-annealed microstructures that visualize the spread of the carbides for 1.5Al–100Cr6 steel in a,a1) and for 1.5Si–100Cr6 steel in b,b1).
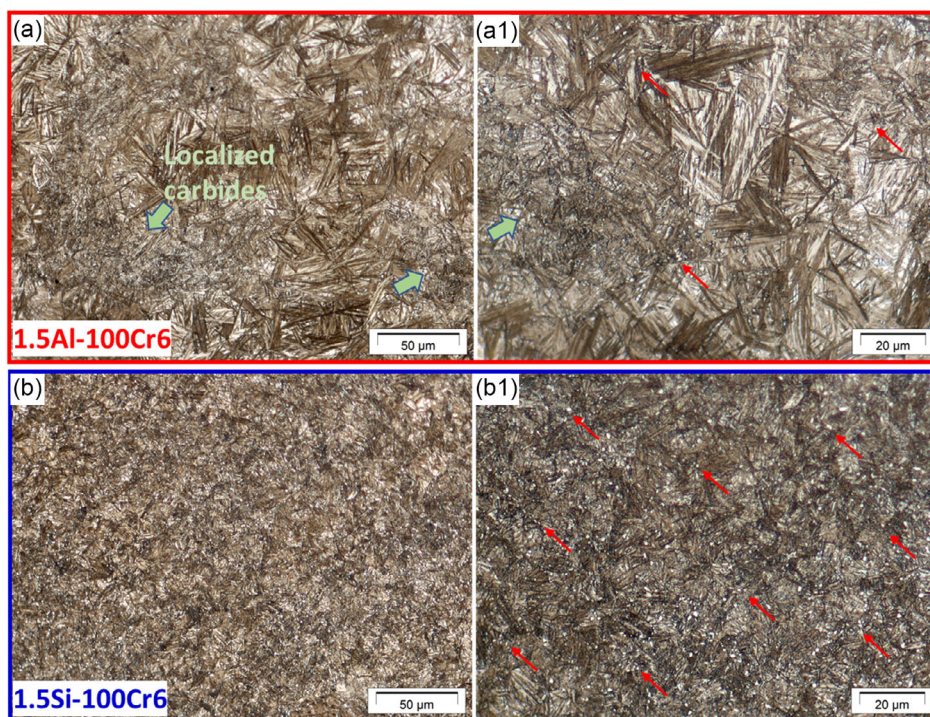
Figure 10. LOM micrographs of the bainitized microstructure for a,a1) 1.5Al–100Cr6 steel and b,b1) 1.5Si–100Cr6 steel. The red arrows refer to the cementite particles and the green arrows to the localized carbides.

to 1.5Si–100Cr6 steel. Furthermore, the carbides are localized over large individual areas in the coarse bainitized microstructure of 1.5Al–100Cr6 steel (green arrows); however, they seem to be randomly distributed and located at several small regions in the fine bainitized microstructure of 1.5Si–100Cr6 steel, which is analyzed in more detail using SEM in the following section. Like the solution-annealed microstructures, the cementite particles (e.g., indicated by red arrows) exist in a larger amount for 1.5Si–100Cr6 steel as compared to 1.5Al–100Cr6 steel (Figure 10a1,b1). Based on the current LOM micrographs, the expected retained austenite could not be resolved.

In **Figure 11**, SEM images of 1.5Al–100Cr6 steel captured in two different regions, that is, a carbide-free zone (Figure 11a,a1,a2) and with localized carbides (Figure 11a',a'1,a'2), as well as for 1.5Si–100Cr6 steel (Figure 11b,b1,b2) are shown at different magnifications. Detailed features of the bainitized microstructures, such as bainite plates and sheaves, retained austenite, carbides, and cementite particles are clearly observed.

In the carbide-free region of 1.5Al–100Cr6 steel, large packets of bainite plates in different orientations and small smooth areas of retained austenite in between are visible, even at relatively low magnification.[23] At higher magnification, the individual bainite sheaves are resolved, and the retained austenite appears mostly as blocks and elongated plates with a size of few micrometers. In the localized carbide region of 1.5Al–1000Cr6 steel (red arrows indicate the carbides/cementite particles), the boundaries between different packets of bainite plates are not fully distinguishable; however, the individual bainite sheaves are still discernible at high magnification. Moreover, in the region with localized carbides, the retained austenite exists predominantly as short plates, small blocks, and films. The size of retained austenite islands in this region is generally smaller than that observed in the carbide-free region.

In contrast to 1.5Al–100Cr6 steel, the different packets of bainite plates in 1.5Si1–00Cr6 steel are hardly visible at low magnification. The cementite particles of 1.5Si–100Cr6 steel are significantly larger than those observed in the localized carbides region of 1.5Al–100Cr6 steel, while the retained austenite appears relatively finer in 1.5Si–100Cr6 steel. However, both variants show an apparently similar amount of retained austenite, being 22% in the 1.5Si–100Cr6 steel[18] and 24% in the 1.5Al–100Cr6 steel. Note that the amounts of retained austenite were determined by XRD and thus represent a more or less integral value of the retained austenite content. The three morphologies, that is, block, plate, and film, are observed in the bainitized microstructure of 1.5Si–100Cr6 steel as well, however, with smaller sizes.
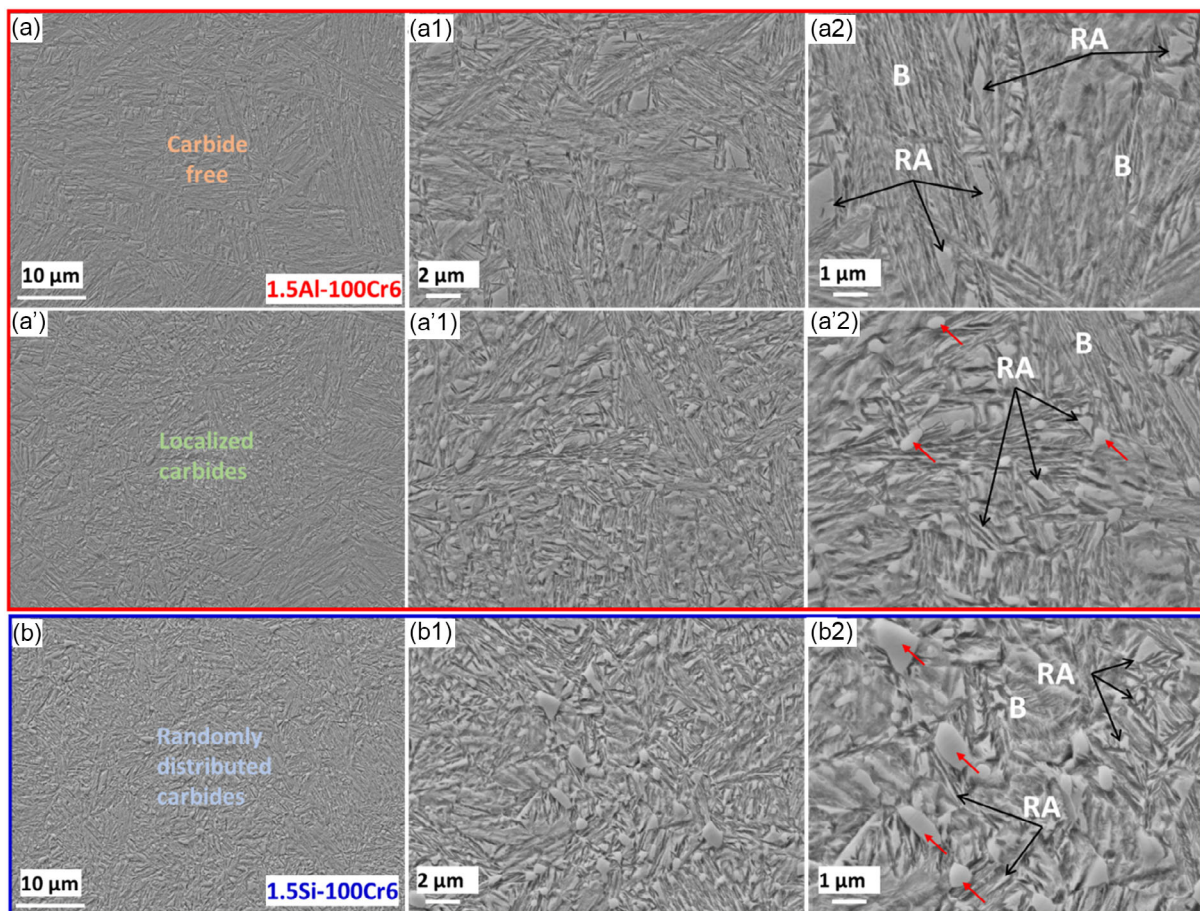
Figure 11. SEM images of the bainitized microstructures. a), a1), a2) taken at different magnifications in a carbide-free region, a'), a'1), a'2) recorded in a region of localized carbides for 1.5Al–100Cr6 steel as well as b), b1), b2) taken at different magnifications for 1.5Si–100Cr6 steel. The red arrows point to carbides/cementite particles, the black arrows point to retained austenite (RA), and the letter B stands for bainite.

**ADVANCED
SCIENCE NEWS**

www.advancedsciencenews.com

**steel
research**
international

www.steel-research.de

According to the SEM micrographs, the bainitized microstructures manifest essential differences between the Al- and Si-alloyed 100Cr6 steels in terms of size and fraction of the microstructural constituents. Compared with 1.5Al–100Cr6 steel, the amount and the size of observed cementite are larger, bainite plates and sheaves are finer, and the retained austenite is smaller in size for the 1.5Si–100Cr6 steel.

The EBSD analysis of bainitized microstructures is represented in **Figure 12**, again confirming the coarser microstructure of 1.5Al–100Cr6 steel, which was also observed by LOM and SEM investigations. The gray scale image quality maps displayed in Figure 12a,b show a slightly darker contrast for Si–1.5100Cr6 steel. The inverse pole figure orientation maps (Figure 12a1, b1) reveal for both steels a microstructure without a pronounced texture. The inverse pole figure orientation maps of bainite (BCC phase) and retained austenite (FCC) for 1.5Al–100Cr6 and 1.5Si–100Cr6 steels are shown in a2, a3 and b2, b3 of Figure 12, respectively. The FCC orientation maps indicate the various orientations of the original austenite grains retained after bainite transformation. It is clear that the coarse prior austenite grain structure of 1.5Al–100Cr6 steel resulted in coarser bainite packets as well as larger bainite plates compared to 1.5Si–100Cr6 steel. Moreover, it seems that not all bainite plates in a bainite packet, which emerge from one austenite grain, have the same orientation. Furthermore, it is clear from both orientation maps of the FCC and BCC phases that the austenite is retained among the growing bainite plates. Thereby, the shape of retained austenite is controlled. The relative fractions of the constituting phases in the measured area were estimated based on their corresponding phase maps displayed in Figure 12a4,b4, respectively. While the retained austenite content measured with EBSD (FCC phase in red) is about 32 vol% for 1.5Al–100Cr6 and is about 24 vol% for 1.5Si–100Cr6, nearly similar values could be detected by XRD for the two steels. Considering the size of the measurement area, only very small, local areas are examined in the EBSD analysis, while the results of the XRD analysis can be assumed to be globally valid. However, the phase maps clearly point out the difference in the morphology of the retained austenite. The EBSD phase maps emphasize the dominating block and plate-shaped retained austenite morphologies in 1.5Al–100Cr6 steel, besides the presence of retained austenite films, possibly where cementite particles are localized, for example, at lower left corner of Figure 12a4 (cementite in yellow). However, the retained austenite in 1.5Si–100Cr6 steel exists mostly as short plates and films, and wherever the retained austenite blocks appear, they are still smaller in size than those observed in 1.5Al–100Cr6 steel.

3.4. Monotonic and Cyclic Deformation Behavior

In addition to the microstructural investigations, the mechanical properties of both steels were analyzed in the bainitized condition. To determine the monotonic deformation behavior, tensile tests were performed. The resulting stress–strain curves are shown in **Figure 13**. For each steel, two tensile tests were performed, which show nearly identical stress–strain curves. However, the fracture surface analyses revealed for the specimen S2 of the 1.5Al–100Cr6 steel a substantially different failure mechanism, caused by a microstructural inhomogeneity. This leads to a smaller elongation at fracture and a slightly smaller tensile strength in relation to S1. Thus, the values obtained for S1 are assumed to be more representative for the material's volume properties. Comparing the two steels, despite the microstructural differences observed, the stress–strain curves yield only small differences in 0.2% yield strength (YS) and ultimate tensile strength (UTS) (see **Table 3**). Moreover, no significant differences in strain hardening can be observed between the two steels, as the stress–strain curves are nearly identical. The elongation at fracture A also shows no differences between the two alloys. The only outlier is the sample S2 of the 1.5Al–100Cr6, which shows a significantly lower value for A due to defect-based failure. In the Young's moduli E of the individual batches, only small differences can be observed, where the 1.5Al–100Cr6 steel has a lower E. Despite the microstructural differences observed, the stress–strain curves yield only small differences in 0.2% yield strength (YS) and ultimate tensile strength (UTS) (see Table 3). Moreover, no significant differences in strain hardening can be observed between the two steels, as the stress–strain curves are nearly identical. Only in Young's modulus E and elongation at fracture A, small differences can be observed, while the 1.5Al–100Cr6 steel has a lower E and a slightly lower A. However, these differences are very small.

In addition to the monotonic deformation behavior, the cyclic deformation behavior of both steels was investigated. Therefore, LITs were performed, and the deformation-induced change in temperature ΔT was measured and analyzed (see **Figure 14**). While 1.5Al–100Cr6 reaches a maximum stress amplitude of 960 MPa, 1.5Si–100Cr6 fractures at $\sigma_a = 1120$ MPa and thus, at a significantly higher cyclic loading. Moreover, at similar stress amplitudes, the 1.5Si–100Cr6 steel exhibits a significantly smaller ΔT, which indicates a less-pronounced cyclic plastic deformation in relation to 1.5Al–100Cr6. Consequently, a higher fatigue strength of the 1.5Si–100Cr6 steel could be assumed.

As shown in another study,[24] the cyclic stress–strain (σ_a–$\varepsilon_{a,p}$) curves obtained in an LIT can be used to roughly estimate the fatigue limit σ_w of a material.[25,26] As ΔT can be used adequately to $\varepsilon_{a,p}$[27] for the analysis of the cyclic deformation behavior, cyclic stress–temperatures (σ_a–ΔT) curves (CSTC) can also be used to estimate σ_w. Consequently, the CSTC of both steels was determined based on the results obtained in LIT. For this purpose, the average value of ΔT was determined for each load step and then versus the stress amplitude in double-logarithmic scale, which is illustrated in **Figure 15**a,c. Note that the stress amplitude at fracture was not considered in the CSTC to exclude effects of macrocrack propagation.

In accordance with another study,[24] two power law functions were fit to each CSTC according to the distinctly different slopes observed at low and high stress amplitudes, respectively, see Figure 15b,d. Considering the different slopes, two regimes can be defined, between which there is a transition area, that cannot be assigned clearly to the power functions. As described in another study,[24] the lower regime represents nearly fully elastic deformation, while the upper regime exhibits significant microplastic deformation and hence can be assigned to the high-cycle-fatigue (HCF) regime. Consequently, the highest stress amplitude that cannot be assigned to the upper regime is used as a rough estimation of σ_w.[24]
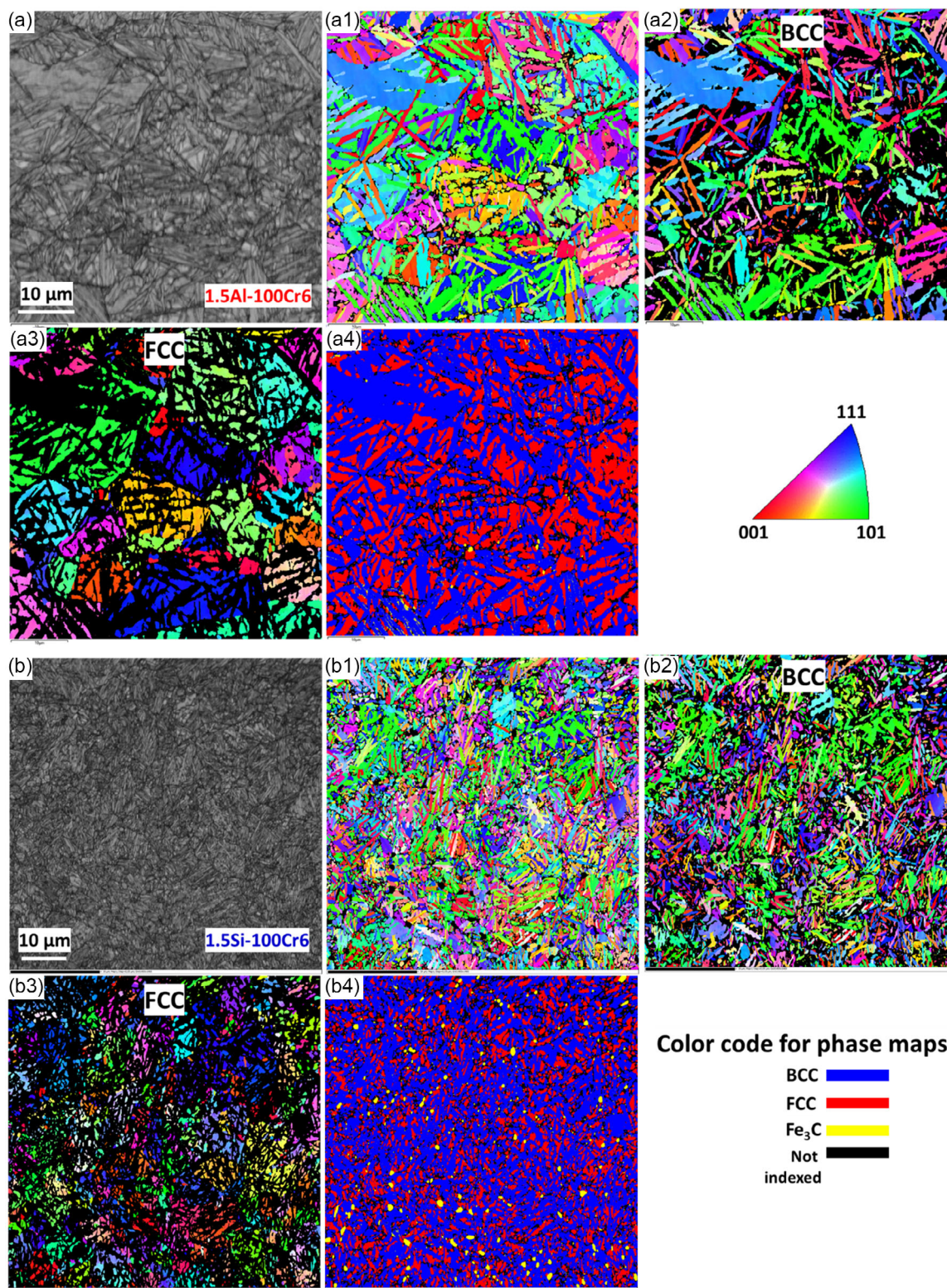
Figure 12. EBSD analysis of the bainitized microstructures. a) and b) grey scale image quality maps, a1,b1) inverse pole figure orientation maps of constituting phases, a2,b2) inverse pole figure orientation maps of FCC phase, and a3,b3) inverse pole figure orientation maps of bcc phase for 1.5Al–100Cr6 and 1.5Si–100Cr6 steels, respectively, as well as a4,b4) phase maps.
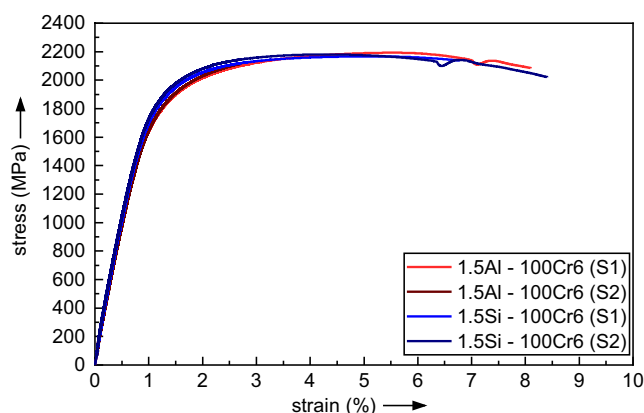
Figure 13. Stress–strain curves obtained in tensile tests at both steels, that is, 1.5Al–100Cr6 and 1.5Si–100Cr6.

Table 3. Characteristic values obtained from tensile tests.

	Test	Ultimate Tensile Strength (UTS) [MPa]	0.2% Yield Strength (0.2%-YS) [MPa]	Elongation at fracture (A) [%]	Young's modulus (E) [GPa]
1.5Al–100Cr6	S1	2193	1668	7.5	200
	S2	2115	1700	2.0	195
1.5Si–100Cr6	S1	2167	1737	6.0	205
	S2	2181	1762	7.6	209
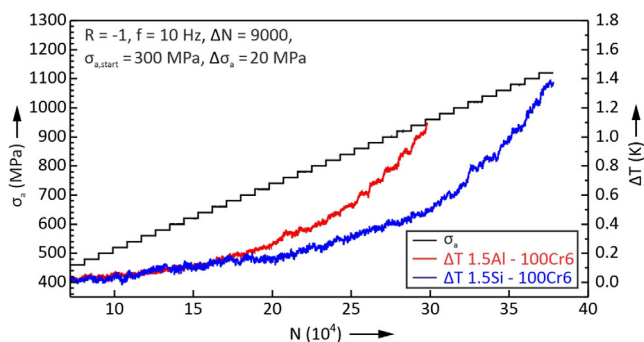
Figure 14. Load increase tests obtained from the steels 1.5Al–100Cr6 and 1.5Si–100Cr6.

The estimated fatigue limit for 1.5Al–100Cr6 is 780 MPa, while for 1.5Si–100Cr6 σ_w was estimated to be 920 MPa. The higher estimated σ_w of 1.5Si–100Cr6 corresponds to the higher stress amplitudes reached in LIT as well as the lower level of ΔT observed. The presented results demonstrate that the 1.5Si–100Cr6 steel has a significantly higher fatigue strength in relation to the variant 1.5Al–100Cr6. Thus, at cyclic loading, the microstructural differences observed substantially influence the deformation behavior, which is in contrast to the tensile tests.

In addition to the LITs, constant amplitude tests were performed to further investigate the cyclic deformation behavior of both steels. Therefore, for each steel, one constant amplitude

test was performed at a high stress amplitude, being higher than the stress amplitude at fracture in the LIT, and at a medium stress amplitude within the region above the transition area of the cyclic stress–temperature curves (see **Figure 16**). In correspondence to the results in the LITs, the 1.5Al–100Cr6 shows at lower stress amplitudes a similar amount of cyclic plastic deformation than 1.5Si–100Cr6. Thus, 1.5Si–100Cr6 shows a higher fatigue life even at higher stress amplitudes. Consequently, the results obtained in constant amplitude tests confirm the results obtained in the LITs.

4. Discussion

4.1. Influence of Al- and Si-Alloying Concepts on Microstructure Evolution of 100Cr6 Steel

The main target of adding Al and Si to the roller-bearing steel 100Cr6 has been achieved in the current study, since the adjusted microstructure of both alloying concepts comprises 22 vol% up to 24 vol% significant amounts of retained austenite. However, further phenomena caused by these alloying concepts have been observed. Usually, the conventional 100Cr6 type steel shows a pearlitic microstructure in the hot-deformed condition, and it can include some secondary cementite at the prior austenite grain boundaries.[28] The presence of secondary cementite networks at the grain boundaries has a detrimental effect on the rolling contact fatigue behavior,[1] and such cementite networks have to be avoided either by adjusting the cooling strategy after hot-deformation[29] or through applying a subsequent annealing treatment to spheroidize the cementite.[30] The processing of the 1.5Al–100Cr6 steel resulted in the formation of secondary cementite at the grain boundaries in the as-forged microstructure, which is attributed to the depletion of Al and the concomitant enrichment of carbide-forming elements, particularly Cr, in the interdendritic regions as it is delineated by the Scheil-solidification calculation and depicted by the MICRESS simulation. On the contrary, the cosegregation of Si in the interdendritic regions observed for the Si-alloying concept significantly reduces the probability of forming secondary cementite at the grain boundaries in the as-forged microstructure of 1.5Si–100Cr6 steel. The retardation of secondary cementite in austenite by a small addition of Si has been reported by Kozeschnik and Bhadeshia[31] and can be explained by the reduction in driving force of cementite precipitation reaction from austenite.

In the solution-treated state, the amount of cementite and carbides strongly depends on the applied austenitization heat treatment. The current results emphasize the additional role of possible segregation on the presence and distribution of cementite and carbides. Although the applied austenitization temperature of 900 °C is higher than the equilibrium temperature for cementite dissolution (A_{cem}) of 1.5Al–100Cr6 ($\approx$860 °C), the microstructure shows some regions containing carbides while other regions are carbide free (Figure 9). Taking into consideration the segregation behavior (shown in Figure 5 and 6) as well as its consequence for the grain boundary cementite (shown in Figure 7), it can be inferred that the corresponding local A_{cem} in segregation-containing regions should be different. **Figure 17**
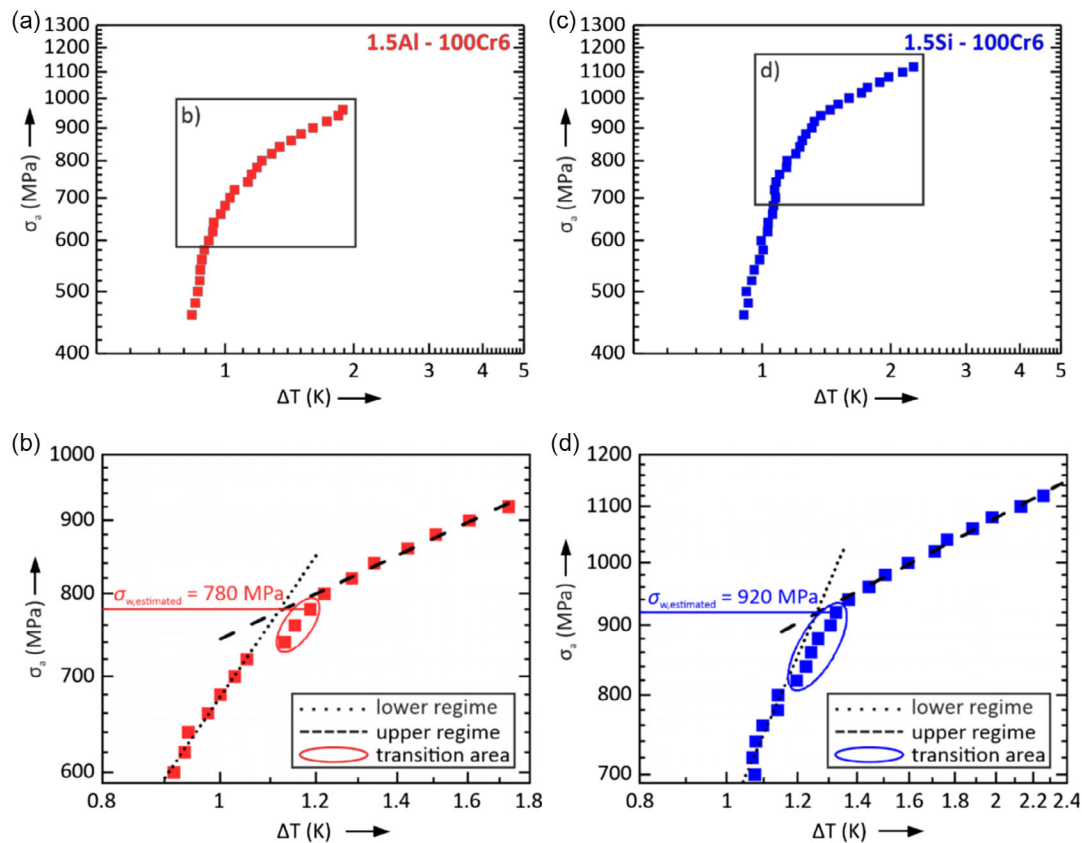
Figure 15. Cyclic stress–temperature curves of the steels a) 1.5Al–100Cr6 and c) 1.5Si–100Cr6 as well as b), d) a respective illustration with a higher resolution including the estimation of fatigue strength $\sigma_{w,estimated}$.
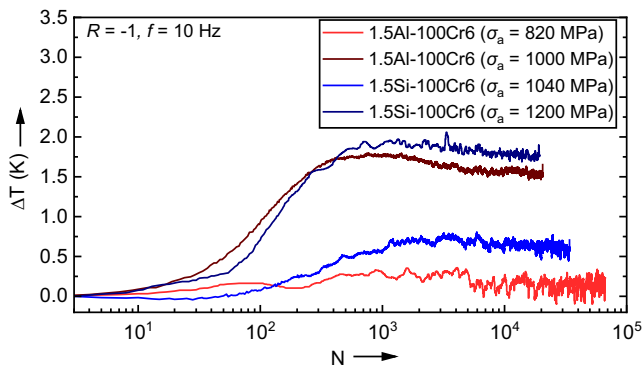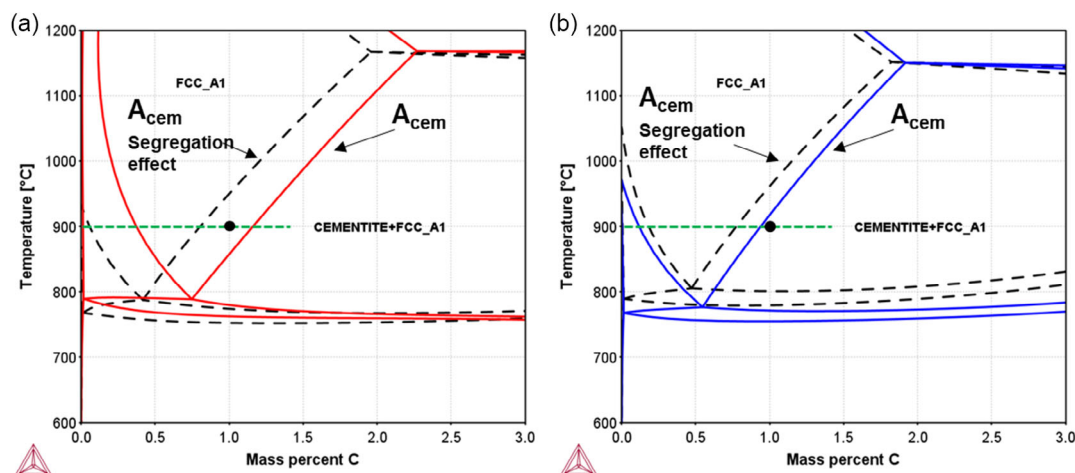

Figure 16. Cyclic deformation curves obtained in constant amplitude tests of the two steels 1.5Al–100Cr6 and 1.5Si–100Cr6 at a high and medium stress.

represents parts of the equilibrium phase diagrams of the Al- and Si-alloying concepts, which are compiled using the original compositions (solid lines) and the composition of the segregated regions based on Scheil-solidification calculations (dashed lines). It is obvious that considering the influence of segregation on the local chemistry leads to an increase in A_{cem} temperature to a higher value than the applied austenitization temperature, which is responsible for the presence of carbide-free and carbide-containing regions. Although the composition of segregated regions of Si-alloying concept increases the local A_{cem}

temperature too, almost no pronounced free and localized carbide regions were observed in the microstructure of 1.5Si–100Cr6 steel, since the applied austenitization temperature is lower than the corresponding A_{cem} temperature either with or without considering the segregation effect. Consequently, for the 1.5Si–100Cr6, the carbides were not dissolved during austenitization.

Furthermore, Al and Si differently affect the dissolution/spheroidization of cementite during austenitization heat treatment. Despite the longer austenitization time of 60 min applied for the 1.5Si–100Cr6 steel compared to only 30 min for 1.5Al–100Cr6 steel, the cementite in the localized carbide regions of 1.5Al–100Cr6 steel appears relatively finer than that observed for the 1.5Si–100Cr6 steel. It is proposed that this behavior is due to the increase of carbon activity in austenite enriched with Si that has a low solubility in cementite. Such high activity of C in austenite retards the dissolution of the existing cementite. Kim and Lee[32] concluded that increasing Si content (>1 wt%) in 100Cr6 retarded the spheroidization of cementite owing to the increase in carbon activity at the cementite/austenite interface, leading to a decrease in the driving force of carbon diffusion from cementite to austenite, which is in agreement with the current observations. **Figure 18** indicates the increase in the carbon activity (calculated by Thermo-Calc) induced by Si-alloying to 100Cr6 steel compared with Al-alloying.

**ADVANCED
SCIENCE NEWS**

www.advancedsciencenews.com

**steel
research**
international

www.steel-research.de

Figure 17. Part of equilibrium phase diagram calculated using Thermo-Calc software considering the original composition (solid line) and the possible shift in phase diagram induced by segregation of alloying elements (dashed line) for: a) 1.5Al–100Cr6 and b) 1.5Si–100Cr6 steels. The nominal carbon content of the investigated steels and the chosen austenitization temperature are indicated by the black dots and green-dashed lines, respectively.
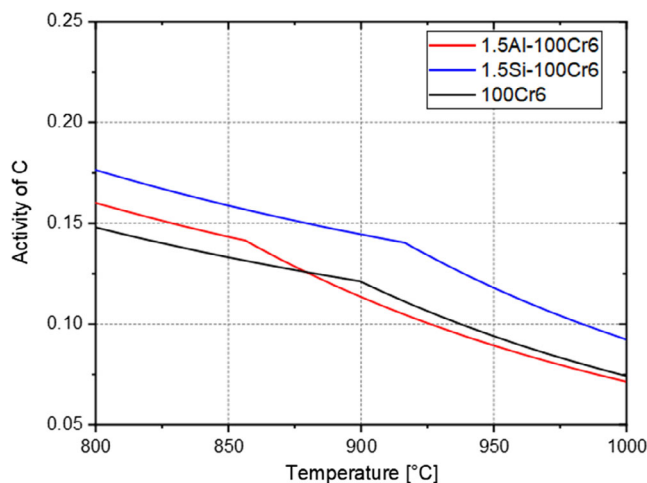
Figure 18. The influence of Al- and Si-alloying concepts on the carbon activity of 100Cr6 steel compiled using Thermo-Calc.

4.2. Role of inherited Microstructure during Heat Treatment

A detailed examination of the microstructures in the bainitized state clearly indicates that the chemical heterogeneity that already arises during casting is inherited as a result of the segregation behavior. Overall, the local enrichment of alloying elements is much more pronounced in the Al-alloyed variant. For example, the Scheil calculation for Mn results in an enrichment in the residual melt from the nominal value from 0.43 to 0.9 wt% Mn or from 1.5 to 3.0 wt% Cr, while the enrichment in the Si-alloyed variant is with 0.6 wt% Mn and 2.4 wt% Cr, respectively, significantly smaller. Added to this is the pronounced negative segregation of the element Al.

Consequently, the EBSD analyses of the bainitic microstructure resulting from both alloying concepts displayed some distinctive characteristics, for example, relative size of bainite packets and sheaves as well as the distribution of cementite

and carbides, which in turn influence the morphology, size, and volume fraction of retained austenite. The different sizes of bainite packets (relatively coarser for Al- than Si-concept) reflect the original, relatively coarser pearlitic microstructure stemmed from the as-forged state of 1.5Al–100Cr6 steel (Figure 7). The bainite transformation from relatively smaller austenite grains in the case of Si concept resulted in the formation of finer bainite plates. Also, the presence of localized carbides-free and carbide-rich regions, explained above by the difference in local A_{cem} temperature induced by segregation, is inherited in the bainitized state of 1.5Al–100Cr6. Moreover, the homogeneous distribution of carbides during austenitization of 1.5Si–100Cr6 is transferred to the bainitized state. As a consequence, the bainite formation for Al and Si alloying concepts starts with different austenite conditions in terms of C level and grain size, which significantly influenced the overall phase transformation kinetics and the corresponding evolved microstructures.

At last, the size of the carbides also differs. While in the 1.5Al–100Cr6 steel a bimodal distribution of the carbides is found with coarse carbides in the order of 1000–2000 nm, which were probably not or only incompletely dissolved during the heat treatment, and carbides in the order of approximately smaller than 500 nm, in the 1.5Si–100Cr6 steel only the coarse carbides of few micrometers in size are present. The coarse carbides in 1.5Si–100Cr6 steel are due to the incomplete dissolution during austenitization.

4.3. Microstructure–Mechanical Behavior Relationship

The described microstructural differences between the two steels lead to nearly identical monotonic properties. However, the LITs reveal pronounced differences in the cyclic deformation behavior as well as in the respective estimated fatigue strengths, being 140 MPa higher for the 1.5Si–100Cr6 variant. The improved fatigue behavior of the 1.5Si–100Cr6 steel was further confirmed by the constant amplitude tests and can be explained by its more

homogenous and refined microstructure in relation to 1.5Al–100Cr6. However, a refined microstructure is also supposed to lead to higher monotonic strength. That the fatigue experiments reveal, in contrast to the tensile tests, pronounced differences might be caused by the higher sensitivity of the fatigue test to microstructural changes.

Furthermore, it could be assumed that the carbide-free zones lead to a higher cyclic plasticity and, thus, a decreased fatigue strength. Moreover, it could be possible that the steels have different austenite stabilities. As the deformation-induced phase transformation depends on the loading conditions, this might explain the different results obtained in tensile and fatigue tests. However, to verify these assumptions, more detailed analyses of the fatigue behavior and the microstructural changes caused by cyclic loading are a prerequisite, which is the objective of future work.

5. Conclusion

The influence of Al and Si alloying on the microstructure development of the roller-bearing steel 100Cr6 during processing as well as on the mechanical properties has been investigated. The thermodynamic and kinetic simulations, as well as light optical, SEM, and EBSD analyses, have been used. The following conclusions can be drawn from the results: 1) Local heterogeneities in the chemical composition already arise during the solidification caused by segregations, which lead to locally different microstructures. These are inherited through the manufacturing process up to the final microstructure after bainitization heat treatment; 2) Overall, the Al-alloyed steel shows more pronounced segregation, which is reflected in the differences of the retained austenite morphology, the carbide distribution, and the microstructure. Compared to the Si-alloyed steel, the Al-alloyed one has coarser austenite grains, coarser bainite packets, and coarser retained austenite islands. The bimodal carbide distribution of the Al-alloyed variant resulted from an inhomogeneous dissolution of the carbides during heat treatment; and 3) The monotonic mechanical properties are on a similar level for both bainitized steels. However, the Si-alloyed steel yields a significantly higher estimated fatigue strength due to the finer microstructure. Consequently, this concept is the more promising approach for a defect-tolerant, high-strength roller-bearing steel.

In future work, the fatigue behavior of the two steels will be analyzed in more detail. In these investigations, a special focus will be on the defect sizes observable in the steels, the evaluation of the defect tolerance, and the influence of the austenite stability on the fatigue lifetime. In this context, the influence of the alloying concept on the austenite stability will be examined.

Conflict of Interest

The authors declare no conflict of interest.

Data Availability Statement

The data that support the findings of this study are available from the corresponding author upon reasonable request.

[1] H. Bhadeshia, *Prog. Mater Sci.* **2012**, *57*, 268.

[2] E. Erişir, Ö. Ararat, O. G. Bilir, *Metall. Mater. Trans. A* **2022**, *53*, 850.

[3] Z. Xu, X. Shen, T. Allam, W. Song, W. Bleck, *Mater. Sci. Eng., A* **2022**, *829*, 142115.

[4] B. Blinn, M. Klein, C. Gläßner, M. Smaga, J. Aurich, T. Beck, *Metals* **2018**, *8*, 220.

[5] W. Bleck, M. Bambach, V. Wirths, in *HSLA Steels 2015, Microalloying 2015 & Offshore Engineering Steels 2015*, Vol. *63* (Ed: TMS), John Wiley & Sons, Inc, Hoboken, NJ **2015**, pp. 97–107.

[6] H. S. Kramer, P. Starke, M. Klein, D. Eifler, *Int. J. Fatigue* **2014**, *63*, 78.

[7] D. Spriestersbach, E. Kerscher, *Int. J. Fatigue* **2018**, *111*, 93.

[8] X. Wang, C. Liu, B. Sun, D. Ponge, C. Jiang, D. Raabe, *Proc. Natl. Acad. Sci. U.S.A.* **2022**, *119*, e2110139119.

[9] E. Yajima, T. Miyazaki, T. Sugiyama, H. Terajima, *Trans. JIM* **1974**, *15*, 173.

[10] B. Clausen, T. Karsch, H.-W. Zoch, in *Bearing Steel Technologies: 11th Volume, Advances in Steel Technologies For Rolling Bearings* (Ed: J. M. Beswick), ASTM International, West Conshohocken, PA **2017**, pp. 343–365.

[11] Z. Xu, J. Li, X. Shen, T. Allam, S. Richter, W. Song, W. Bleck, *Metals* **2021**, *11*, 1888.

[12] C. Sidoroff, M. Perez, P. Dierickx, D. Girodin, in *Bearing Steel Technologies: 10th Volume Advances in Steel Technologies For Rolling Bearings* (Ed: J. M. Beswick), ASTM International, West Conshohocken, PA **2015**, pp. 1–37.

[13] DIN EN ISO 683-17:2015-02, Für eine Wärmebehandlung bestimmte Stähle, legierte Stähle und Automatenstähle_-Teil_17: Wälzlagerstähle (ISO_683-17:2014); Deutsche Fassung EN_ISO_683-17:2014, Beuth Verlag GmbH, Berlin.

[14] H. L. Yi, Z. Y. Hou, Y. B. Xu, D. Wu, G. D. Wang, *Scr. Mater.* **2012**, *67*, 645.

[15] *Alloying: Understanding the Basics* (Ed: J. R. Davis), ASM International, Materials Park, OH **2001**.

[16] T. Sourmail, M. Millot-Méheux, *Mater. Sci. Technol.* **2016**, *32*, 1126.

[17] A. Lünenbürger, *Zum Unwandlungs- und Verformungsverhalten bainitisch- austenitischer Siliziumstähle*, Universität Karlsruhe (TH), Karlsruhe **1991**.

[18] P. Ostermayer, K. Burkart, B. Blinn, H. Surm, B. Clausen, T. Beck, *Mater. Test.* **2022**, *64*, 1298.

[19] DIN EN ISO 6892-1:2017-02, Metallische Werkstoffe_- Zugversuch_-Teil_1: Prüfverfahren bei Raumtemperatur (ISO_6892-1:2016); Deutsche Fassung EN_ISO_6892-1:2016, Beuth Verlag GmbH, Berlin.

**ADVANCED
SCIENCE NEWS**

www.advancedsciencenews.com

**steel
research**
international

www.steel-research.de

[20] G. Biallas, A. Piotrowski, D. Eifler, *Fatigue Fract. Eng. Mater. Struct.* **1995**, *18*, 605.

[21] P. Starke, D. Eifler, *Mater. Test.* **2009**, *51*, 261.

[22] T. Allam, W. Bleck, C. Klinkenberg, B. Kintscher, U. Krupp, J. Rudnizki, *J. Mater. Res. Technol.* **2021**, *15*, 292.

[23] J. Tian, G. Xu, H. Hu, X. Wang, H. Zurob, *J. Mater. Res. Technol.* **2020**, *9*, 13594.

[24] B. Blinn, M. Ley, N. Buschhorn, R. Teutsch, T. Beck, *Int. J. Fatigue* **2019**, *124*, 389.

[25] B. Jost, M. Klein, T. Beck, D. Eifler, *Int. J. Fatigue* **2018**, *110*, 225.

[26] D. Görzen, H. Schwich, B. Blinn, W. Song, U. Krupp, W. Bleck, T. Beck, *Int. J. Fatigue* **2021**, *144*, 106042.

[27] P. Starke, F. Walther, D. Eifler, *Adv. Eng. Mater.* **2010**, *12*, 276.

[28] W. Song, U. Prahl, Y. Ma, W. Bleck, *Steel Res. Int.* **2018**, *89*, 1800028.

[29] P. GEMBALOVA, J. BORUTA, E. GRYCZ, K. M. CMIEL, *Arch. Civ. Mech. Eng.* **2007**, *7*, 21.

[30] S. Chattopadhyay, C. M. Sellars, *Acta Metall.* **1982**, *30*, 157.

[31] E. Kozeschnik, H. K. D. H. Bhadeshia, *Mater. Sci. Technol.* **2008**, *24*, 343.

[32] K.-H. Kim, J.-S. Lee, *Mater. Sci. Technol.* **2012**, *28*, 50.

2200804 (16 of 16)